Program Digest, 2019 IEEE International Ultrasonics Symposium (IUS)
Glasgow, Scotland, October 6-9, 2019

3D reconstruction of handheld data by SAFT and the influence of measurement inaccuracies

Fabian Krieg*†, Sayako Kodera†, Jan Kirchhof*†, Florian Römer*, Alexander Ihlow†, Sergey Lugin*, Ahmad Osman*‡, Giovanni Del Galdo*§
*Fraunhofer IZFP, Saarbrücken, Germany, †Technische Universität Ilmenau, Germany,
‡University of Applied Sciences, htw saar, Saarbrücken, Germany, §Fraunhofer IIS, Ilmenau, Germany
Contact: *fabian.krieg@tu-ilmenau.de*

***Abstract*—In this paper, we investigate the influence of measurement inaccuracies of assisted handheld ultrasound measurements on reconstructions with the Synthetic Aperture Focusing Technique (SAFT). The assistance system tracks the position of the handheld transducer with a camera. The accuracy of such a tracking is inferior to the accuracy of positioning systems in automated measurement setups. Further, due to the manual transducer movement, the coupling of the transducer can vary, which is an additional error source. We carry out two simulation studies that investigate each of the error sources separately. We evaluate the simulations by computing the (Generalized) Contrast to Noise Ratio on C-images of the SAFT reconstruction. The results show that the SAFT reconstruction is sensitive even to small model mismatches due to tracking or coupling errors, demonstrating that monitoring of these effects is required for reliable reconstruction. An exemplary SAFT reconstruction of handheld measurement data is shown.**

***Index Terms*—SAFT; ultrasound NDT; handheld measurements; assistance systems;**

I. Introduction

Ultrasonic flaw detection is an important modality in Non-Destructive Testing (NDT). Despite an inreasing automation of the measurement process, manual inspection remains necessary for difficult measurement tasks, or when the quantity of the components for inspection is too small to implement a specialized automated measurement setup. Compared to automated measurements, these tests are less reproducible and traceable, depending heavily on the test engineer's experience. In order to support these engineers and increase reproducibility, assistance systems have been developed [1]. The manually moved ultrasound probe is tracked by a camera, allowing the assistance system to capture the positional information of the probe on the specimen surface together with the measured A-scan. In combination, this can be used to provide feedback to the engineer during inspection in the form of a real-time image. To enhance the quality of this image, signal processing, e.g., real-time reconstruction can be applied. In automated ultrasound NDT, the Synthetic Aperture Focusing Technique (SAFT) [2, 3] is the state of the art reconstruction algorithm. However, to the best of our knowledge few investigations on the topic of SAFT processing for handheld data have been conducted. In [4] intermediate results on the development of a system for the investigation of tendon-ducts in concrete are shown. This system uses the SAFT algorithm in combination with manual data acquisition. No hints regarding the algorithmic implementation of the processing are given.

In our previous work, we proposed a SAFT formulation that is capable of being used for handheld measurement data [1, 5]. In this paper, we investigate the influence of measurement inaccuracies on this proposed reconstruction scheme. In contrast to automated measurement setups, where the positioning accuracy is in the sub-millimeter range, a camera-based tracking system is prone to estimation errors. Moreover, a manually moved transducer can experience varying coupling, further degrading the measurements. We carry out two simulation studies where the impact of the two aforementioned error sources on the reconstruction are separately investigated. The impact is measured using the Contrast to Noise ratio (CNR) and the Generalized Contrast to Noise Ratio (GCNR) [6].

II. Data model for the Synthetic Aperture Focusing Technique calculation

In this section, we briefly revisit the data model as formulated in [5]. This approach has been favored for its computational benefits. However, applying this approach to manual inspections, where the measurement positions are not necessarily sampled equidistantly in spatial domain, introduces an additional quantization error to the reconstruction. For an in-depth investigation of the computational gains see [5].

Consider a pulse-echo ultrasound setup. We assume the propagation medium to be isotropic and homogeneous with speed of sound c_0. Each measurement vector, sampled at the sampling frequency f_s is given as $\boldsymbol{s}(\mathsf{x_t}, \mathsf{y_t}) \in \mathbb{R}^{\mathsf{N_t} \times 1}$, where $\mathsf{x_t}, \mathsf{y_t}$ are indices denoting the spatial measurement position. The measurements are recorded at the equispaced positions $x_t = \mathsf{x_t} d_x$ and $y_t = \mathsf{y_t} d_y$ where d_x and d_y represent the step-width of the measurement in x-direction and y-direction, respectively, and a total number of $N_x N_y$ measurements are collected. For brevity of notation we perform the reconstruction on the same sampling grid. Let $\boldsymbol{r}(\mathsf{x_r}, \mathsf{y_r}) \in \mathbb{R}^{\mathsf{N_z} \times 1}$ denote one vector of the reconstruction. Each of its values corresponds to the estimated reflectivity of the specimen at the point (x_r, y_r, z_r) where $x_r = \mathsf{x_r} d_x$ and $y_r = \mathsf{y_r} d_y$ and $z_r = -\mathsf{z} d_z$. The step-width

Fabian Krieg is funded by DFG under the project "CoSMaDU". This work was supported by the Fraunhofer Internal Programs under Grant No. Attract 025-601128.

d_z along the depth-axis is given as $d_z = \frac{c_0}{2f_s}$. The transducer resides at $z = 0$. The propagation time of an ultrasonic wave from a transducer to a reflector and back is given by

$$t_{tr} = \frac{2}{c_0}\sqrt{(x_t - x_r)^2 + (y_t - y_r)^2 + z_r^2}. \tag{1}$$

The SAFT reconstruction yields an approximation to the specimen's reflectivity based on a superposition of echoes that relate to the same coordinates in the reconstruction [2]. The reconstruction is given as

$$\boldsymbol{r}(\mathsf{x_r}, \mathsf{y_r})[\mathsf{z}] = \sum_{\forall \mathsf{x_t}, \mathsf{y_t}} a(\phi)\boldsymbol{s}(\mathsf{x_t}, \mathsf{y_t})\left[\mathrm{nint}\left(t_{tr} f_s\right)\right], \tag{2}$$

where $\boldsymbol{x}[\cdot]$ denotes a scalar entry of the vector, $\mathrm{nint}(\cdot)$ is the rounding operation and $a(\phi)$ is the apodization function depending on the angle ϕ between surface normal and the propagation path from $(x_t, y_t, 0)$ to (x_r, y_r, z_r). We limit ourselves to a rectangular apodization here [3].

We can deduce a matrix-vector product from (2) as

$$\boldsymbol{r} = \boldsymbol{M}\boldsymbol{s}, \tag{3}$$

where $\boldsymbol{M} \in \mathbb{R}^{\mathsf{N_z N_x N_y} \times \mathsf{N_t N_x N_y}}$ and $\boldsymbol{r} \in \mathbb{R}^{\mathsf{N_z N_x N_y} \times 1}$ and $\boldsymbol{s} \in \mathbb{R}^{\mathsf{N_t N_x N_y} \times 1}$. Consequently, $\boldsymbol{s}$ becomes the concatenation of all measurement vectors, where each measurement vector (A-scan) holds $\mathsf{N_t}$ time samples.

Due to the shift invariance in x- and y-direction in (1) and the equidistant spatial sampling grid, the matrix $\boldsymbol{M}$ is a block matrix composed of submatrices corresponding to a certain $(\mathsf{i} = \mathsf{x_t} - \mathsf{x_r}, \mathsf{j} = \mathsf{y_t} - \mathsf{y_r})$ that are arranged in a 2-Level Toeplitz structure [5]. For fixed i, the set of defining blocks $\boldsymbol{M}_{\mathsf{i,j}} \in \mathbb{R}^{\mathsf{N_z} \times \mathsf{N_t}}$ for all j (in a slight abuse of notation) leads to the following mapping:

$$\boldsymbol{M}_{\mathsf{i,j}} \mapsto \boldsymbol{M}_{\mathsf{i}}(\boldsymbol{M}_{\mathsf{i,j}}) = \begin{bmatrix} \boldsymbol{M}_{\mathsf{i},0} & \boldsymbol{M}_{\mathsf{i},-1} & \cdots & \boldsymbol{M}_{\mathsf{i},-\mathsf{N_x}+1} \\ \boldsymbol{M}_{\mathsf{i},1} & \boldsymbol{M}_{\mathsf{i},0} & & \boldsymbol{M}_{\mathsf{i},-\mathsf{N_x}+2} \\ \vdots & & \ddots & \vdots \\ \boldsymbol{M}_{\mathsf{i},\mathsf{N_x}-1} & \boldsymbol{M}_{\mathsf{i},\mathsf{N_x}-2} & \cdots & \boldsymbol{M}_{\mathsf{i},0} \end{bmatrix}, \tag{4}$$

with $\boldsymbol{M}_{\mathsf{i}} \in \mathbb{R}^{\mathsf{N_x N_z} \times \mathsf{N_x N_t}}$. Accordingly, a mapping for the complete $\boldsymbol{M}$ iterating over i as $\boldsymbol{M}_{\mathsf{i}} \mapsto \boldsymbol{M}(\boldsymbol{M}_{\mathsf{i}})$ can be defined.

From this it follows that the overall matrix $\boldsymbol{M}$ is completely defined by the set of $(2\mathsf{N_x} - 1)(2\mathsf{N_y} - 1)$ blocks $\boldsymbol{M}_{\mathsf{i,j}}$. It can be seen from (1) that for the given problem the block Toeplitz structure even becomes symmetric, i.e. $\boldsymbol{M}_{\mathsf{i}} = \boldsymbol{M}_{-\mathsf{i}}$ and $\boldsymbol{M}_{\mathsf{i,j}} = \boldsymbol{M}_{\mathsf{i},-\mathsf{j}}$ for all i, j, reducing the number of required defining matrices further.

In the given handheld scenario, we need to compute the reconstruction on a subset of the full measurement grid, performing the reconstruction in a progressive manner by updating it with each newly measured A-scan. The update is performed as

$$\boldsymbol{r} \leftarrow \boldsymbol{r} + \boldsymbol{M}^{(\mathsf{v})}\boldsymbol{s}(\mathsf{x}, \mathsf{y}), \tag{5}$$

where $\boldsymbol{M}^{(\mathsf{v})} \in \mathbb{R}^{\mathsf{N_z N_x N_y} \times \mathsf{N_t}}$ is the v-th block column of $\boldsymbol{M}$ referring to the measurement at (x, y) and $\mathsf{v} = \mathsf{x} + \mathsf{y}\mathsf{N_x}$. The indices ($\mathsf{x}$ and y) are obtained by rounding the measurement position tracked by the position measurement system to the nearest point of the desired observation grid. Due to the 2-Level Toeplitz structure of the block matrices in $\boldsymbol{M}$ the formation of $\boldsymbol{M}^{(\mathsf{v})}$ reduces to the correct indexing of the generating blocks $\boldsymbol{M}_{\mathsf{i,j}}$. The transformation of a block row index u and block column index v to the indices i, j of a generating element $\boldsymbol{M}_{\mathsf{i,j}}$ is given in [5]. This scheme allows to perform the reconstruction in an arbitrary order and a grid can be deduced beforehand from the capability of the tracking system.

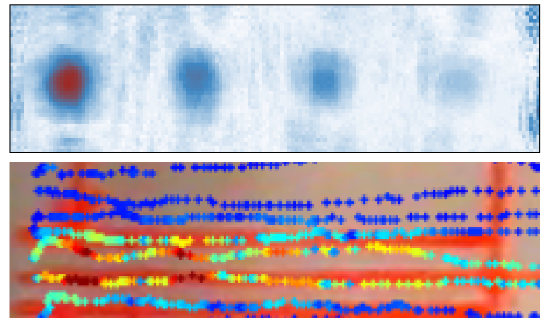

Fig. 1. Exemplary SAFT reconstruction of a manual measurement, top: C-image of the reconstruction, bottom: measurement points on the surface.

III. Measurements

In this section, we shortly present an example reconstruction result from manual measurements. The measurements were collected from an aluminium specimen with four flat bottom holes with diameters decreasing from $5\,\mathrm{mm}$ to $2\,\mathrm{mm}$. The measurements were taken manually and tracked by a camera based assistance system [1]. Measurements, sampled at $20\,\mathrm{MHz}$, were taken from 509 scan positions. In Fig. 1, the upper image shows a C-image of the reconstruction, the lower image depicts the sampling points on the specimen surface. The size of the holes decreases from left to right. The reconstruction was performed on a grid with a spacing of $0.5\,\mathrm{mm}$ based on (5). The C-image spans an area of $7.35\,\mathrm{cm} \times 2.05\,\mathrm{cm}$. The C-image was calculated as the maximum value of each reconstruction vector $\boldsymbol{r}(\mathsf{x_r}, \mathsf{y_r})$.

IV. Investigation of the Measurement Errors

In this section, we present the simulation studies which investigate the influence of measurement errors on the SAFT imaging quality.

A. Simulation settings

In Table I the simulation settings are summarized. A sketch is given in Figure 2, a C-image of a reference reconstruction in Figure 5(a), all reconstructions are computed according to (5). We compute each single measurement vector by calculating the time of flights between the transducer and all defect positions, quantizing them to the temporal sampling grid, but not assuming a lateral grid in x and y, using Dirac-spike for each defect and then convolving a Gaussian pulse along the temporal axis. The transducer beam spread is modeled as a simple rectangular window in angular domain.

TABLE I
PARAMETERS OF THE SIMULATED MEASUREMENTS

material	aluminium
defect model	point scatterer
scenario size	$2\,\mathrm{cm} \times 2\,\mathrm{cm} \times 3\,\mathrm{cm}$
defect location	4 defects at depth $2\,\mathrm{cm}$ to $2.5\,\mathrm{cm}$
sampling	$0.5\,\mathrm{mm}$ in x,y; sampling frequency $80\,\mathrm{MHz}$
pulse	center frequency $5\,\mathrm{MHz}$ / $\lambda = 1.26\,\mathrm{mm}$

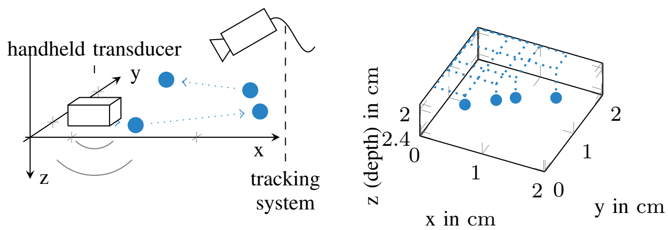

Fig. 2. Left: Sketch of the measurement setup, Right: Scatterer locations of the simulated scenario.

B. Metrics

We choose the Contrast to Noise Ratio (CNR) and the Generalized Contrast to Noise Ratio (GCNR) as metrics for tracking the degradation of the C-images of the reconstruction due to the tracking/coupling errors. They have shown to align better with the visual impression of the degradation than more general metrics, such as mean square error or structural similarity. Both metrics are based on comparing the statistics of a true positive region and a true negative region in the image. Here, the true positive region is chosen to be those pixels, which are above a $3\,\mathrm{dB}$ threshold of the maximum amplitude in the reference reconstruction shown in Figure 5(a). This results in 16 pixels per reconstruction in the positive class and 1584 pixels in the negative class, rising the need to draw the amplitudes from many realizations to allow estimating statistically conclusive measures.

The CNR is calculated as

$$\mathrm{CNR} = \frac{|\mu_+ - \mu_-|}{\sqrt{\sigma_+^2 + \sigma_-^2}}, \tag{6}$$

where μ_+, μ_-, σ_+, σ_- are the mean of positive and negative class pixel amplitudes and the standard deviation of positive and negative class pixel amplitudes, respectively. The amplitudes are collected from 100 realizations for each parameter set.

The GCNR [6] is a more robust alternative to the CNR. It is given by

$$\mathrm{GCNR} = 1 - \int \min\left(p_+(x), p_-(x)\right) \mathrm{d}x, \tag{7}$$

where $p_+(x)$ and $p_-(x)$ are the probability density functions of each class. We collect the pixel amplitudes of both classes over 100 realizations for each parameter set and approximate the probability density functions by a 10 bin histogram over the amplitude range of both classes for each class.

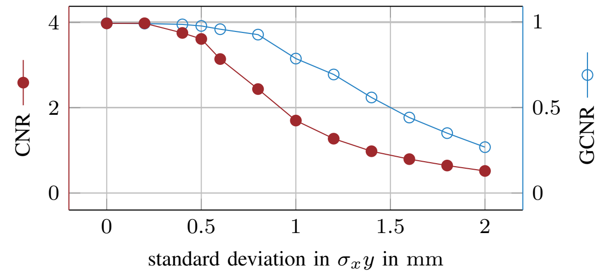

Fig. 3. Degradation of the C-images of the reconstruction for increasing simulated position tracking error in x and y

C. Position tracking inaccuracies

a) Model: To depict the impact of inaccuracies in the position tracking system we choose an approach where we pick 160 scans, which is a $10\,\%$ of the total number of points on the sampling grid, uniformly distributed at random. We then calculate the data for exactly these transducer positions. To augment errors in the tracking, each position information is then distorted by a random offset, drawn from a 2D Gaussian distribution. The distorted amplitudes are then fed to the SAFT reconstruction framework, which inherently maps them to the sampling grid for performance reasons again.

b) Results: In Figure 3 the metrics are evaluated for varying standard deviation $\sigma_{xy} = \sigma_x = \sigma_y$ of the Gaussian distribution distorting the tracked x, y position of the simulated transducer. In Figure 5(d)-5(f) C-images of example realizations are provided. With increasing error the noise in the C-images increases and the peak amplitudes decline. At $\sigma_{xy} = 0.5\,\mathrm{mm}$ the visual impact is already significant, at a GCNR of 0.976 and a CNR decrease of $0.42\,\mathrm{dB}$. For $\sigma_{xy} = 1\,\mathrm{mm}$, at a GCNR of 0.78 and a CNR decrease of $3.69\,\mathrm{dB}$, the reconstructions are already unusable. Comparing this to the wavelength of the pulse of $1.26\,\mathrm{mm}$ shows that the impact is significant even below half the wavelength.

D. Decoupling of the transducer

a) Model: In automated inspection in immersion technique, the coupling of the transducer and positioning with respect to the specimen surface are consistent for all A-scans. In contrast, manual measurements in contact technique record imperfect coupling and surface variations. We model these effects as displacement in the z-direction. To remove the influence of subsampling and position quantization from the results, the fully sampled dataset is used here, resulting in 1600 scans contributing for each reconstruction. The z coordinate of the transducer is chosen as a random Gaussian distributed variable at the data synthesization stage. The reconstruction is then performed from these measurements, erroneously assuming all measurements to be recorded at $\mathrm{z} = 0$.

b) Results: In Figure 4 the metrics are evaluated for varying standard deviation σ_z of the Gaussian distribution distorting the z position of the simulated transducer. In Figure 5(a)-5(c) C-images of example realizations are provided.

In relation to the wavelength of the pulse carrier frequency the performance of the reconstruction reduces much faster than

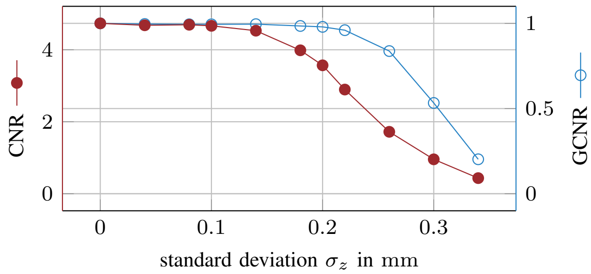

Fig. 4. Degradation of the C-images of the reconstruction for increasing simulated position tracking error in z

for the lateral tracking error. At $\sigma_z = 0.2\,\mathrm{mm}$ the GCNR is at 0.98 and CNR decrease of $1.23\,\mathrm{dB}$, for $\sigma_z = 0.3\,\mathrm{mm}$ the performance decreased to GCNR $= 0.53$ and CNR by $6.95\,\mathrm{dB}$.

Compared to the position tracking mismatch in x and y, the variation in z has a far more severe impact with respect to the wavelength. In real world measurements such small deviations could be induced by uneven surfaces or a slight accidental slant of the transducer. While this probably does not compromise the C-image representation of the raw measurement data significantly, it needs to be considered for SAFT post-processing of the data. Countermeasures could include detecting the deviations from the A-scans by tracking the backwall / frontwall echos or by using the envelopes of the A-scans as input to the SAFT-processing, with the drawback of a significantly reduced focusing capability.

Comparing the C-images of both the deviation in x, y and deviation in z and the according values of GCNR and CNR it becomes clear that both metrics do not precisely track the visual impression of the C-images. The GCNR is only slighty decreased where the amount of background artifacts is visually prominent, as background noise does not influence the measure under a given threshold. The CNR decreases faster but can not be used for quanititative comparison of both error sources. In conclusion, both metrics represent only an indication that needs to be combined with additional measures such as a visual inspection of the reconstructed image's quality.

V. Conclusion and Outlook

We have investigated and quantified the impact of erroneously estimating the transducer position on the imaging quality of the SAFT-reconstruction. Tracking errors of the lateral position of the transducer resulted in a significant decrease of the imaging quality at a standard deviation of the tracking error in the range of half the wavelength of the pulse. More surprisingly, a wrong assumption of the transducer position perpendicular to the ideal flat specimen surface resulted in a visual impact at as little as 0.1 the wavelength, with only a small increase in the deviation leading to totally unusable results of the reconstruction. Still, reconstruction from manual measurement data is possible as shown in Sec. III.

For future work we intend to tackle with these error sources by correcting the tracking error iteratively in post-processing using estimated reflector positions deduced from the SAFT-processing. Furthermore, we are investigating whether the coupling and deviation in z-direction can be detected during the measurement, allowing to weight the contribution of measurement vectors to the reconstruction according to their conclusiveness.

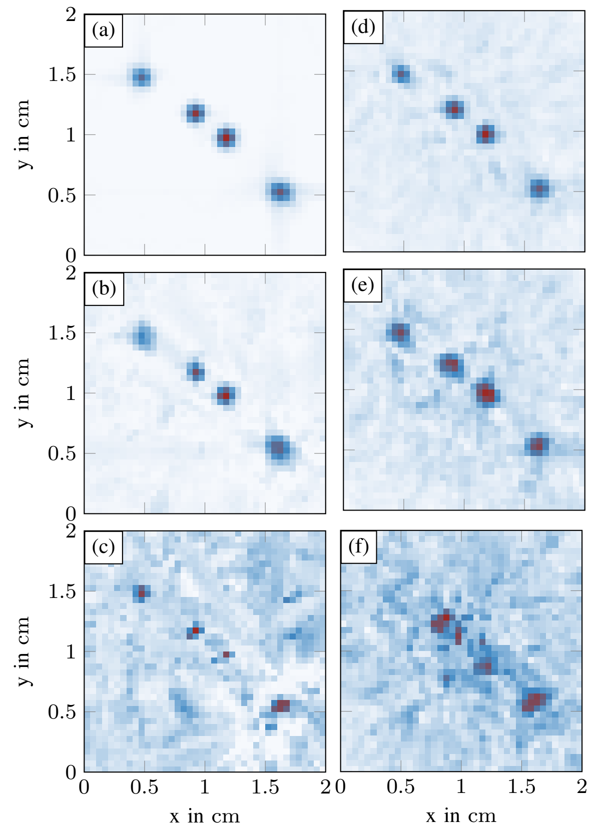

Fig. 5. C-images of the reconstruction for (a)-(c) fully sampled, with (a) $\sigma_z = 0\,\mathrm{mm}$, (b) $\sigma_z = 0.2\,\mathrm{mm}$, (c) $\sigma_z = 0.3\,\mathrm{mm}$; (d)-(f) 160 uniformly randomly taken samples with augmented tracking error with (d) $\sigma_{xy} = 0\,\mathrm{mm}$, (e) $\sigma_{xy} = 0.5\,\mathrm{mm}$, (f) $\sigma_{xy} = 1\,\mathrm{mm}$

References

[1] F. Krieg, S. Lugin, J. Kirchhof, A. Ihlow, T. Schwender, G. Del Galdo, F. Römer, and A. Osman. SAFT processing for manually acquired ultrasonic measurement data with 3D smartInspect. In *Int. Symp. on SHM and NDT*, 2018.

[2] M. Spies, H. Rieder, A. Dillhöfer, V. Schmitz, and W. Müller. Synthetic aperture focusing and time-of-flight diffraction ultrasonic imaging—past and present. *Journ. of NDE*, 31:310–323, 2012.

[3] F. Krieg, J. Kirchhof, F. Römer, A. Ihlow, G. del Galdo, and A. Osman. Implementation issues of 3D SAFT in time and frequency domain for the fast inspection of heavy plates. In *IEEE IUS*, 2017.

[4] K. Mayer, M. Krause, M. Ibrahim, and M. Schubert. Requirements for a small size ultrasonic imaging system for inspection of concrete elements. In *19th WCNDT*, 2016.

[5] F. Krieg, J. Kirchhof, F. Römer, R. Pandey, A. Ihlow, G. del Galdo, and A. Osman. Progressive Online 3-D SAFT Processing by Matrix Structure Exploitation. In *IEEE IUS*, Oct 2018.

[6] A. Rodriguez-Molares, O. M. Hoel Rindal, J. D'hooge, S.-E. Måsøy, A. Austeng, H. Torp. The Generalized Contrast-to-Noise Ratio. In *IEEE IUS*, 2018.